Lu, G., Richmond, A. D., Lühr, H., Paxton, L. (2016): High-latitude energy input and its impact on the thermosphere. - *Journal of Geophysical Research*, *121*, 7, pp. 7108—7124.

DOI: http://doi.org/10.1002/2015JA022294

AGU PUBLICATIONS

JGR

Journal of Geophysical Research: Space Physics

RESEARCH ARTICLE
10.1002/2015JA022294

Key Points:
- The polar cap is not the primary location of high-latitude energy input
- Thermospheric mass density anomalies do not always coincide with direct local energy dissipation
- Thermosphere dynamics redistributes mass globally through gradient-wave adjustment

Correspondence to:
G. Lu,
ganglu@ucar.edu

Citation:
Lu, G., A. D. Richmond, H. Lühr, and L. Paxton (2016), High-latitude energy input and its impact on the thermosphere, *J. Geophys. Res. Space Physics*, *121*, 7108–7124, doi:10.1002/2015JA022294.

Received 21 DEC 2015
Accepted 1 JUL 2016
Accepted article online 7 JUL 2016
Published online 23 JUL 2016

High-latitude energy input and its impact on the thermosphere

G. Lu[1], A. D. Richmond[1], H. Lühr[2], and L. Paxton[3]

[1]High Altitude Observatory, National Center for Atmospheric Research, Boulder, Colorado, USA, [2]Helmholtz Center Potsdam, GFZ German Research Center for Geosciences, Potsdam, Germany, [3]Applied Physics Laboratory, Johns Hopkins University, Laurel, Maryland, USA

Abstract This paper presents a quantitative assessment of high-latitude energy input and its partitioning in the polar cap by synthesizing various space and ground-based observations during the 17 January 2005 geomagnetic storm. It was found that Joule heating is the primary form of magnetospheric energy input, especially during active times when the hemispheric-integrated Joule heating can be an order of magnitude larger than the hemispheric-integrated auroral power. Most of magnetospheric energy is dissipated in the auroral zone rather than in the polar cap. On average, only about 22–25% of the total hemispheric energy input is dissipated into the polar cap region bordered by the convection reversal boundary (CRB) and the poleward auroral flux boundary (FXB). The impact of high-latitude energy input was also investigated to unveil the causal relationship between Joule heating and the formation of polar cap mass density anomalies. Our numerical simulation demonstrated that thermosphere dynamics readily redistributes composition, temperature, and mass through upwelling and atmospheric gravity waves. The polar cap mass density anomalies observed by the CHAMP satellite during the storm were largely a result of large-scale atmospheric gravity waves. Therefore, an increase in local thermospheric mass density does not necessarily mean there is direct energy input.

1. Introduction

The high-latitude ionosphere plays a key role in solar-terrestrial energy transfer processes. Through solar wind-magnetosphere interaction, a fraction of the solar wind energy is transmitted into the magnetosphere and subsequently dissipated into the high-latitude ionosphere to power the aurora and other geomagnetic phenomena. Energy input from the magnetosphere to the high-latitude ionosphere has a major impact on the dynamics and chemistry of the thermosphere [e.g., *Rishbeth*, 1991; *Prölss*, 1995, 1997; *Schunk and Sojka*, 1996; *Fuller-Rowell et al*., 1997; *Richmond and Lu*, 2000]. Therefore, an accurate specification of high-latitude energy input is critical to understand how solar and magnetospheric forcing affects the upper atmosphere.

The high-latitude region includes both the polar cap, where the magnetic field lines are directly connected to the solar wind, and the auroral zone, where the field lines are considered closed, that is, both ends of the field lines are connected to the Earth. Joule heating and auroral precipitation are the two main forms of magnetospheric energy input. Efforts to estimate high-latitude energy dissipation traditionally rely on empirical models, for example, the models of auroral precipitation by *Hardy et al*. [1985, 1991], *Fuller-Rowell and Evans* [1987], *Newell et al*. [2009, 2010], *Mitchell et al*. [2013], and *Zhang and Paxton* [2008], and the models of Joule heating by *Foster et al*. [1983], *Chun et al*. [2002], and *Weimer* [2005]. With the improvement in data coverage and advancement in data assimilation techniques, the high-latitude energy input can also be estimated for specific events by combining various observations [e.g., *Waters et al*., 2004; *Richmond et al*., 1988; *Emery et al*., 1990; *Lu et al*., 1996, 1998, 2001]. These efforts have revealed that both Joule heating and auroral precipitation mainly reside in the auroral zone. However, more recent studies show that the polar cusp, in addition to the auroral zone, is a region of significant energy input [e.g., *Knipp et al*., 2011]. Some studies [e.g., *Huang et al*., 2014] even suggest that the polar cap, rather than the auroral zone, is the primary location of energy input. It has also been pointed out that the height distribution of the heat deposition is important for the high-altitude density response, with heat deposited at higher altitudes having a stronger influence on the high-altitude density than the same amount of heat deposited at lower altitudes [*Deng et al*., 2011; *Huang et al*., 2012]. These recent studies have prompted new interests in energy partition over the high-latitude ionosphere.

Indeed, large neutral mass density enhancements have been observed by the CHAMP satellite near the polar cusp, accompanied by intense small-scale field-aligned currents (FACs) as first reported by *Lühr et al*. [2004]. It has been suggested that Alfvénic waves associated with small-scale FACs produce Ohmic heating that causes thermospheric upwelling [*Lühr et al*., 2004]. But the relationship between density enhancement and local energy dissipation is far from conclusive. A statistical survey of the CHAMP data over a 4 year period of 2002–2005 found that nearly 50% of polar cap density enhancement events did not show any concurrent increase in energy input as represented by FACs [*Liu et al*., 2010]. What would then be the cause of density enhancement in the absence of direct energy dissipation? To answer this question would require a full, quantitative understanding of the energetic coupling between the ionosphere and thermosphere, including realistic specification of energy input over the entire high-latitude ionosphere, and the chemical and dynamical processes responsible for the thermospheric density redistribution. Several modeling studies have shown the important role of thermospheric dynamics in altering the horizontal distribution of temperature and density [e.g., *Richmond and Matsushita*, 1975; *Millward et al*., 1993; *Burns et al*., 1995; *Crowley et al*., 1996, 2006; *Deng et al*., 2009]. It is well known that traveling atmospheric disturbances (TADs) launched by high-latitude thermospheric heating can produce transient density structures that are not directly linked to local heating [e.g., *Forbes et al*., 2005; *Bruinsma and Forbes*, 2010]. Density structures associated with TADs are typically observed at midlatitude and low latitude, and they propagate equatorward at a speed close to local sound speed, e.g., 500–1000 m/s in the upper thermosphere [*Mayr et al*., 1990; *Bruinsma and Forbes*, 2009, and references therein]. However, the manner in which TADs may affect specific observed high-latitude density structures has not been determined [*Liu et al*., 2010]. Some studies have attributed changes in mean molecular mass as an important contributing factor to neutral mass density variations [e.g., *Lei et al*., 2010; *Qian et al*., 2010; *Thayer et al*., 2012; *Liu et al*., 2014].

Because of the limited field of view and the cadence of measurements by an individual platform, e.g., satellites or ground-based instruments, estimation of high-latitude energy input is commonly obtained through statistical analysis of data collected over a long period of time and then averaged with regard to geophysical conditions. Although the average patterns of high-latitude ionospheric convection and auroral precipitation are good representations of solar wind/magnetosphere conditions in terms of average behavior, they are inadequate to replicate individual storm events owing to the dynamic nature of the high-latitude ionosphere. The need for accurate specification of high-latitude energy input has been clearly demonstrated by *Fuller-Rowell et al*. [1999]. In that study the authors had to arbitrarily rotate the peak Joule heating location based on an empirical model by 70° in order to reproduce the polar cap density holes observed by the Satellite Electrostatic Triaxial Accelerometer. *Huang et al*. [2014] also noted that the energy input based on the *Weimer* model [*Weimer*, 2005] not only misplaced the locations of the peak energy dissipation but also underestimated the total energy input when compared with the Defense Meteorological Satellite Program (DMSP) satellite measurements. In order to unravel the array of dynamic processes responsible for the global- and regional-scale features in the thermosphere and their relationship to solar wind/magnetosphere conditions, it is critically important to specify the high-latitude energy input as accurately as possible both in space and in time. This importance has been illustrated in the recent study by *Liuzzo et al*. [2015], who assessed quantitatively how the different high-latitude inputs may affect thermospheric winds and temperature.

The purpose of this paper is to quantify the high-latitude energy input and its impact on the thermosphere during a specific storm event on 17 January 2005. This was one of several events during which some peculiar thermospheric density anomalies were observed in the polar region by the CHAMP satellite [*Liu et al*., 2010]. We first use the assimilative mapping of ionospheric electrodynamics (AMIE) procedure to characterize the height-integrated Joule heating and auroral energy dissipation by combining the various observations from both space- and ground-based instruments, with a particular focus on the energy input to the polar cap region. We then proceed with numerical simulation of the thermospheric response to the high-latitude energy input using the well-established thermosphere-ionosphere-electrodynamics general circulation model (TIEGCM) developed at the National Center for Atmospheric Research (NCAR). By applying realistic time-dependent high-latitude energy input derived from AMIE, we show that the TIEGCM is capable of reproducing thermospheric density anomalies observed by CHAMP. The underlying physical processes responsible for the observed density anomalies are discussed in light of the model simulation.

2. Results

2.1. High-Latitude Energy Input

The AMIE procedure is specifically designed to obtain time-dependent global distributions of high-latitude ionospheric convection and auroral precipitation by synthesizing various ground- and space-based measurements [*Richmond and Kamide*, 1988]. Over the years the AMIE algorithm has undergone several updates to improve its ability to ingest new types of data [e.g., *Lu et al*., 1998, 2001]. For this case study, the data input to AMIE includes magnetic field perturbations at 215 ground magnetometer stations worldwide, ion drift measurements from the DMSP satellites (F13 and F15), and from the Super Dual Auroral Radar Network (SuperDARN) high-frequency coherent scatter radars. Energy flux and mean energy of auroral precipitating electrons are obtained from the in situ particle measurements by the DMSP and NOAA-POES (NOAA-15, 16, and 17) satellites. In addition, auroral images from the Global Ultraviolet Imager (GUVI) on board the Thermosphere-Ionosphere Mesosphere Energetics and Dynamics satellite and from the Special Sensor Ultraviolet Spectrographic Imager (SSUSI) on board the DMSP-F16 satellite are also used to determine the energy and energy flux of precipitating auroral electrons. Another important data input to AMIE comes from the CHAMP magnetometer (smoothed to 20 s resolution), which helps constrain the AMIE outputs of electromagnetic fields especially along the satellite track. The ground magnetometer data are averaged to 1 min resolution, and the SuperDARN data have a 2 min cadence. The satellite ion drift and in situ particle data are averaged to 15 s resolution, while the GUVI and SUSSI auroral images are binned to 1° in latitude and 0.3 h in local time. The AMIE outputs are saved at a 5 min cadence, and the time window for the satellite data is ±3 min of the model time. The spatial resolution of the AMIE outputs is determined by the order of the polynomial functions as well as the total number of basis functions. The current version employs a set of 244 basis functions, which allow a representation of features of the electrodynamic fields down to about 1.5° in latitude and 10° in longitude. Accordingly, the AMIE spatial grid is set to 1.67° in latitude and 10° in longitude.

The region poleward of the auroral zone is referred as the polar cap where geomagnetic field lines are connected with the interplanetary magnetic field (IMF). The polar cap boundary is thus also considered as the boundary that separates open field lines (i.e., field lines that have one end rooted on the Earth and the other end connected to the IMF) and closed field lines (i.e., field lines with both ends on the Earth). The morphology of the polar cap is strongly controlled by the interaction between the solar wind and magnetosphere so that it serves as an important indicator of magnetospheric dynamics. Changes in the polar cap size have been used to infer changes in magnetic energy storage and release during substorms [e.g., *Baker et al*., 1997; *Kamide et al*., 1999]. However, identifying the polar cap boundary is not a simple task, which depends on what methodology is being applied and how the boundary is defined. Several different observational methods have been developed in the past to determine the polar cap boundary. A direct (and arguably, most accurate) method to identify the polar cap boundary is based on particle spectrometers aboard polar-orbiting satellites such as DMSP. Automated algorithms have been developed by *Newell et al*. [1996] to classify the various plasma regimes by analyzing the detailed energy spectrograms of precipitating electrons and ions. The main disadvantage of this method is the limited spatial coverage due to the lack of adequate polar-orbiting satellites. There are also a number of indirect methods to identify the polar cap boundary. One commonly used indirect method is based on satellite-borne auroral imagers, in which the polar cap boundary is defined as the location where the auroral luminosity falls below a certain threshold value [e.g., *Brittnacher et al*., 1999; *Kauristie et al*., 1999; *Baker et al*., 2000; *Longden et al*., 2010; *Hubert et al*., 2010]. This method has a great advantage of global coverage and high temporal cadence but suffers from large uncertainties since the exact relationship between auroral emissions and the polar cap boundary has not been fully established. Other indirect methods include the poleward boundary of auroral electrojets and the region-1 currents inverted from ground magnetometers [*Akasofu and Kamide*, 1976; *Mishin*, 1990], the estimate of auroral boundaries from small-scale FAC intensity [*Xiong and Lühr*, 2014], the equatorward edge of HF radar backscatter [*Milan et al*., 1999, 2003], the Doppler spectral width boundary measured by the SuperDARN radar measurements [*Chisham and Freeman*, 2004; *Chisham et al*., 2005], and the convection reversal boundary from SuperDARN and DMSP [e.g., *Sotirelis et al*., 2005; *Chen et al*., 2015]. In this study, we apply three different boundaries as proxies for the polar cap boundary: (1) the convection reversal boundary (CRB), defined as the most poleward boundary between 60° and 80° MLAT where the north-south component of the *E* field flips sign at a given magnetic local time (MLT); (2) the poleward auroral flux boundary (FXB), defined as the location where the energy flux drops by a factor of e^{-1} of its peak value at a given MLT; and (3) the circle boundary at a constant

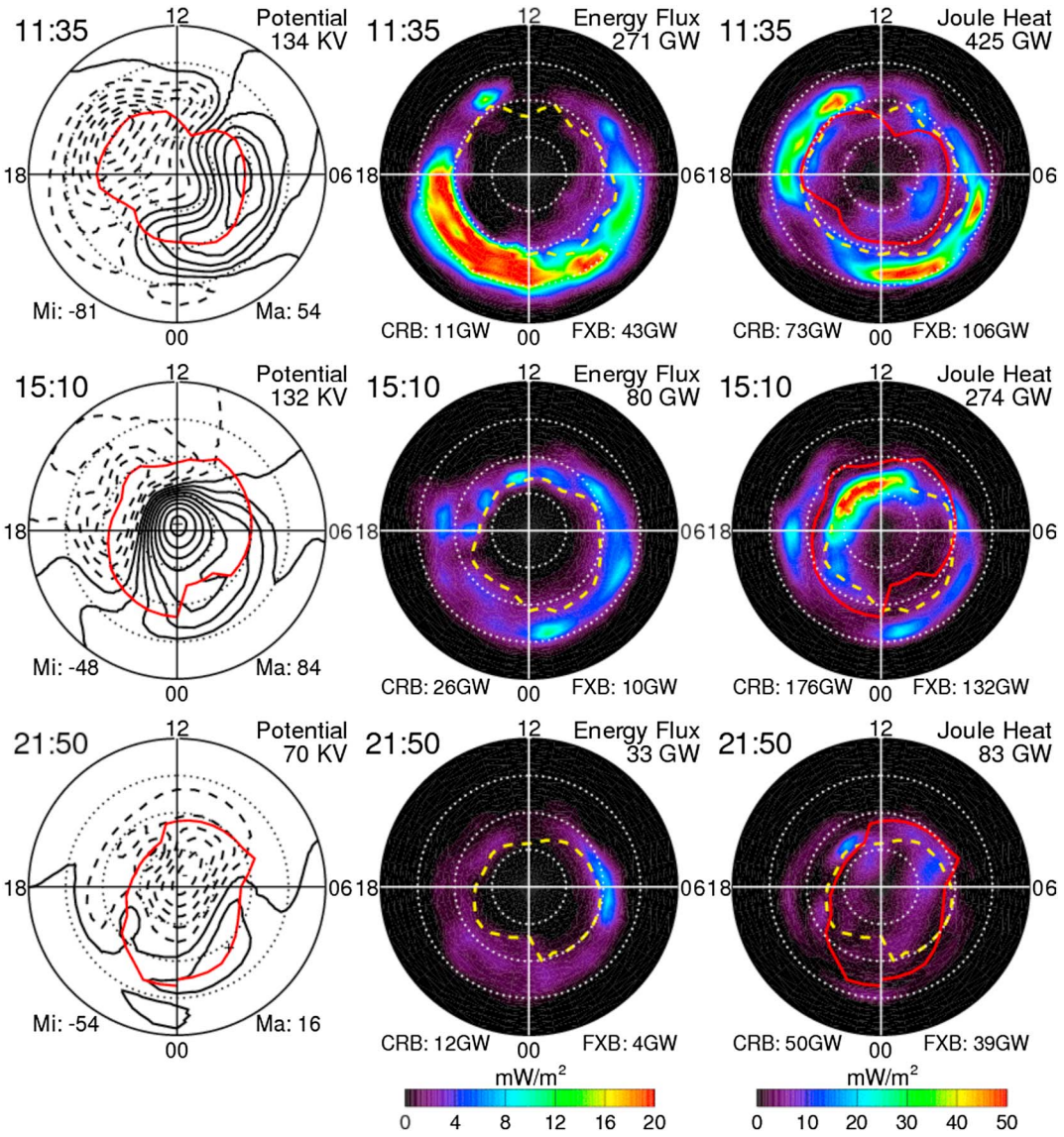

Figure 1. AMIE patterns of convection, auroral precipitating electron energy flux, and height-integrated Joule heating over the Northern Hemisphere at (top row) 11:35 UT, (middle row) 15:10 UT, and (bottom row) 21:50 UT, respectively. The patterns are plotted in magnetic latitude versus magnetic local time coordinates, with the center of the pattern corresponding to the magnetic North Pole. The red line represents the convection reversal boundary (CRB), and the yellow dashed line indicates the poleward auroral flux boundary (FXB).

MLAT of 78°. Though this 78° MLAT is somewhat an arbitrary choice, as discussed in the next section, it is commensurate with the identification of the polar cap mass density anomaly, which is defined as an increase in mass density poleward of |78°| MLAT that is more than 20% above the prevailing background value [e.g., *Liu et al.*, 2010].

Figure 1 shows samples of AMIE outputs at selected UT times on 17 January 2005. Figure 1 (top row) shows the Northern Hemispheric patterns of ionospheric convection, auroral precipitating electron energy flux, and the height-integrated Joule heating at 11:35 UT, and Figure 1 (middle and bottom rows) shows the similar AMIE patterns at 15:10 UT and 21:50 UT, respectively. The red solid line corresponds to the CRB, and the yellow dashed line represents the FXB. Our identification of the FXB is analogous to the poleward boundary of auroral emissions based on the Ultraviolet Imager (UVI) aboard the Polar satellite [*Baker et al.*, 2000]. According to *Baker et al.* [2000], the poleward auroral emission boundary was better defined using a normalized flux ratio of 0.30 with respect to the peak UVI auroral emission intensity at each MLT than using a fixed

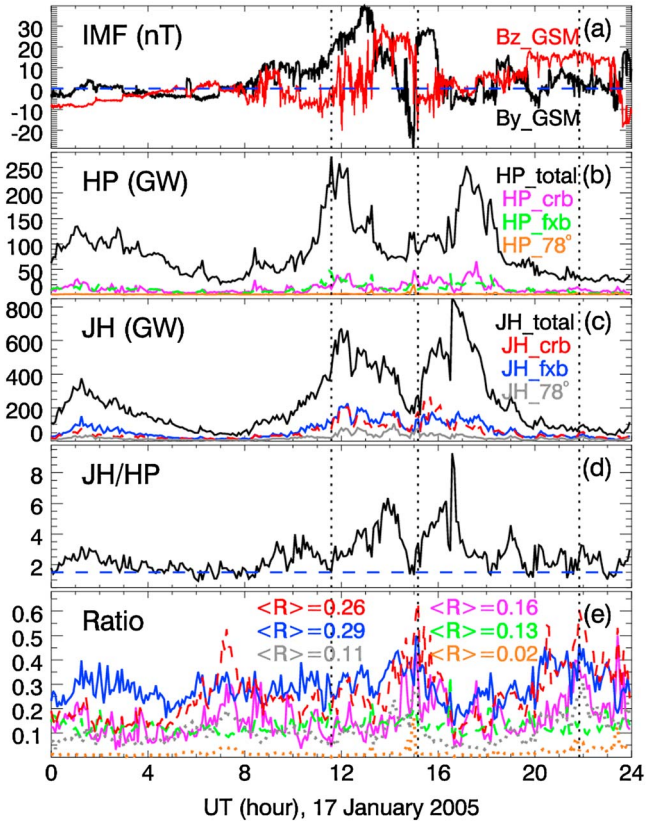

Figure 2. Time series of (a) the IMF B_y and B_z components. (b) HP_total in black, HP_crb in magenta, HP_fxb in green, and HP_78° in brown, (c) JH_total in black, JH_crb in red, JH_fxb in blue, and JH_78° in grey, (d) the ratio of JH_total over HP_total, and the blue dashed line corresponds to a ratio value of 1.5, and (e) the ratio of the polar cap auroral power and Joule heating over the respective hemispheric power for the different polar cap boundaries, and $<R>$ represents the mean value of the different ratios. The vertical dotted lines mark the times when the hemispheric auroral power peaks at 11:35 UT, and when the ratio of JH_crb/JH_total exceeds 0.6 at 15:10 UT and 21:50 UT.

flux threshold, although there was a standard deviation error of approximately 1° in latitude between the UVI and DMSP defined poleward auroral boundaries in the evening sector. *Sotirelis et al.* [2005] also noted that the CRB nearly coincides with the DMSP defined open-closed boundary at local noon but shifts equatorward by ~1° near dawn and dusk. This 1° offset, however, is smaller than the latitude grid size of AMIE and, therefore, should not have a significant effect on our investigation. By comparing the red and yellow contour lines in the Joule heating patterns, the difference between the CRB and FXB can be as large as 10° in some MLT sectors. The resulting difference in the calculated polar cap power based on these two different boundaries should give us a range of variability. The Joule heating and auroral power integrated poleward of the CRB (FXB) are defined as JH_crb (JH_fxb) and HP_crb (HP_fxb), respectively, and their values are given at the lower left (right) corner of the corresponding patterns. The Joule heating and auroral power integrated above 50° MLAT are defined as JH_total and HP_total, respectively, and their values are shown in the upper right corner of the patterns. The difference between the hemispheric power (i.e., JH_total and HP_total) and the polar cap power (i.e., JH_crb or JH_fxb and HP_crb or HP_fxb) is the energy input into the auroral zone. Similarly, Joule heating and auroral energy input above the 78° MLAT circular polar cap boundary are denoted as JH_78° and HP_78°, respectively. Their values (not listed in Figure 1) are smaller than the corresponding polar cap powers based on the CRB and FXB since these boundaries generally lie equatorward of the 78° MLAT circle.

Figure 2 shows the variations of the various energy inputs as defined above, together with the IMF B_y and B_z components over the period of 17 January 2005. The high-latitude energy input is strongly modulated by the IMF orientation: both Joule heating and auroral precipitation increase during southward IMF and decrease during northward IMF. HP_total has a minimum value of ~30 GW and a maximum value of ~270 GW. For JH_total, its minimum value is of ~50 GW and its maximum is of ~850 GW. The ratio of JH_total over HP_total varies from about 1.5 during quiet time to over 9 during active time. Thus, Joule heating is the more significant energy input compared to auroral power. This is consistent with previous findings. For example, *Lu et al.* [1996, 1998] found that, on average, the hemispheric-integrated Joule heating is about twice the hemispheric-integrated auroral power. *Knipp et al.* [2004] estimated the hemispheric-integrated Joule heating and auroral power based on empirical formulas, and their calculations yielded an average daily value of 95 GW for Joule heating and 36 GW for auroral power over solar cycle 22–23. Other theoretical and empirical estimates also indicated that Joule heating exceeds auroral power by a factor of 2 to 6 [e.g., *Akasofu*, 1981; *Ahn et al.*, 1983, 1989].

High-latitude energy input is usually estimated over the entire hemisphere or over the globe. So far, there has been no systematic assessment on the energy partition in the polar cap with respect to the total hemispheric energy input. Motivated by recent interests in the polar cap energy dissipation, this study takes a first step in that direction. As shown in Figure 2e, the fraction of energy input over the polar region is mostly less than 40% of the total hemispheric energy input. The average energy partition over the polar cap ranges from 11% to 29% for Joule dissipation, and even smaller for auroral precipitation (ranging from 2% to 16%), depending on which polar cap boundary is applied. In terms of total energy input (e.g., the sum of Joule heating and auroral power), the average polar cap energy partition (not shown in Figure 2) is 25% when applying the CRB, 22% for the FXB, and 8% for the 78° MLAT circular boundary.

The vertical dotted lines in Figure 2 correspond to the times when HP_total peaks at 11:35 UT, and when the ratio of JH_crb/JH_total exceeds 0.6 at 15:10 UT and 21:50 UT, respectively. At 11:35 UT, IMF B_z is about −2 nT and B_y is about 20 nT. The corresponding ionospheric convection pattern (Figure 1, top row) consists of two cells that are asymmetric about the noon-midnight meridional plane due to the large B_y effect. At 15:10 UT, shortly after B_z has turned from ~25 nT to −4 nT, the convection pattern (Figure 1, middle row) becomes highly distorted, with a dominant positive (clockwise) cell centered at the magnetic North Pole. The auroral precipitation is much weaker compared to that at 11:35 UT when the IMF has persisted southward for several hours. At 21:50 UT, the IMF changes to northward, with $B_z \sim 15$ nT and $B_y \sim 2$ nT, and the convection pattern (Figure 1, bottom row) is dominated by a negative potential cell centered around the magnetic North Pole, and there is no convection reversal between 60° and 80° MLAT in the prenoon sector. As a result, the polar cap boundary in the prenoon sector is simply an extrapolation of the CRB near dawn and local noon, which places the CRB about 5–10° equatorward of the FXB in the prenoon sector. The CRB on the nightside is also farther equatorward of the FXB in the same location, extending as low as 63° MLAT near local midnight. The size of the polar cap shrinks substantially when IMF is northward. Therefore, the CRB in this case would not be a good representation of the polar cap boundary. As shown in Figure 2, the large ratio of JH_crb/JH_total takes place only when IMF B_z is northward and the overall energy input is very small, with HP_total typically less than 50 GW and JH_total less than 100 GW.

Our estimation of polar cap energy input depends on which polar cap boundary is applied. For the case at 15:10 UT, the CRB places the entire dayside region of enhanced Joule heating as part of the polar cap, whereas the FXB nearly coincides with the peak Joule heating. As a result, the calculated polar cap powers based on the CRB and FXB are quite different: 26 GW for HP_crb versus 10 GW for HP_fxb, and 176 GW for JH_crb versus 132 GW for JH_fxb. Correspondingly, the ratio of the polar cap Joule heating versus the hemispheric Joule heating is 0.65 for JH_crb/JH_total and 0.48 for JH_fxb/JH_total. Situations like this call for further examination to determine which polar cap boundary is most appropriate under the given condition. Note that, at 15:10 UT, IMF B_z has turned from northward to southward just about 10 min earlier and B_y is about 20 nT. The AMIE convection pattern shows large eastward converging flows in the postnoon sector. Large Joule heating is found in the region of strong converging flows (and thus large electric fields), whereas the CRB is located more than 5° farther equatorward of the main heating region. The FXB, on the other hand, resides just equatorward of the peak Joule heating in the postnoon sector. A number of previous observational studies [e.g., *Knipp et al*., 2011; *Lühr et al*., 2004] have shown that the dayside cusp is a region of large energy input and heating. Although no DMSP satellites passed the region of intense Joule heating at that UT time to directly measure the plasma properties there, it is reasonable for us to assume this region to be the dayside cusp for the given IMF condition. Since the cusp is located at the equatorward edge of open magnetic field lines [*Newell and Meng*, 1988], the FXB should more suitably represent the polar cap boundary on the dayside in this case. As a comparison, if one applies the constant 78° MLAT circle as the polar cap boundary in this case, it would yield 1 GW for HP_78° and 74.7 for JH_78°, and a ratio of 0.01 for HP_78°/HP_total and 0.27 for JH_78°/JH_total.

It should be noted that the CRB and the FXB are used merely as measures of the polar cap size, and they may not coincide with the boundary between open and closed field lines. However, the identification of the true open-closed boundary requires detailed measurements of precipitating particle energy spectra from satellites such as DMSP at all local times simultaneously, which is practically impossible. Taking advantage of the global nature of the AMIE patterns, the polar cap boundary as defined by the CRB and/or FXB should afford us a systematic assessment of the partition of energy input over the polar cap versus that into the auroral zone.

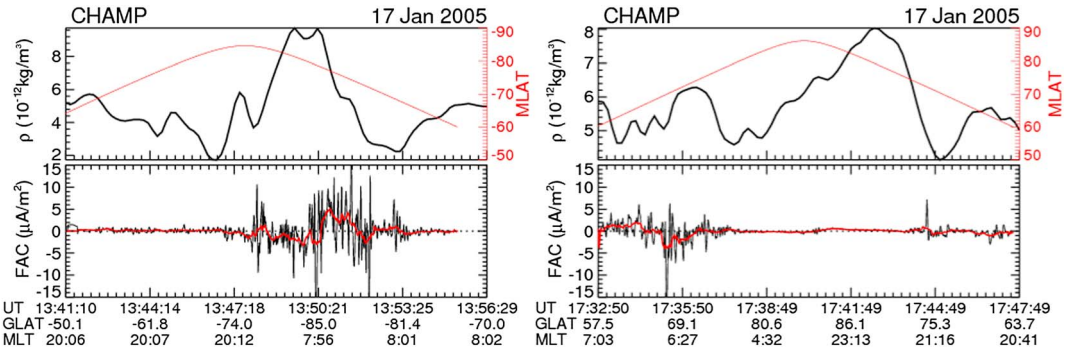

Figure 3. CHAMP neutral mass density and field-aligned currents (left column) over the southern polar region from 13:41 to 13:56 UT and (right column) over the northern polar region from 17:32 to 17:47 UT. The red lines in Figure 3 (top row) indicate the corresponding magnetic latitude of the satellite trajectories, and the red lines in Figure 3 (bottom row) are the 20 s running average of FACs.

2.2. Impact on the Thermosphere

The ionosphere and thermosphere are a tightly coupled system through the complex energy and momentum exchanges between ions and neutrals. The difficulty of simulating thermospheric response in first-principle models lies largely in specifying the magnitude, spatial distribution, and temporal evolution of the high-latitude energy input [e.g., *Fuller-Rowell et al*., 1999]. Coupled with realistic high-latitude electrodynamic outputs from AMIE, we show below the TIEGCM simulation of the 17 January 2005 storm event that features prominent polar cap density anomalies as described in *Liu et al*. [2010].

The TIEGCM [*Richmond et al*., 1992; *Qian et al*., 2013] is a global model of the thermosphere-ionosphere system, extending from ~97 km to about 500–800 km altitude (depending on solar activity). In this study we use the latest high-resolution version of the model which has a horizontal resolution of 2.5° × 2.5° in geographic latitude and longitude and a vertical resolution of one fourth scale height, with a total of 59 constant pressure levels ZP from −7 to 7, where ZP = ln(P/P_0), and P_0 is a reference pressure of 50 μPa. The model incorporates aeronomical, dynamical, and electrodynamical processes that are appropriate for these regions. The model's lower boundary is specified by climatological migrating and nonmigrating tides based on the Global Scale Wave Model (GSWM) [*Hagan and Forbes*, 2002, 2003]. The upper boundary inputs to the model include the solar UV and EUV fluxes, energetic particle precipitation, and polar ionospheric electric fields or convection. For the coupled AMIE-TIEGCM simulation in this case, two of the model upper boundary conditions, namely, auroral precipitation and ionospheric convection, are derived from AMIE. The 5 min AMIE outputs are spatially and temporally interpolated to TIEGCM's grids as it steps in time. The model time step is 1 min for quiet geomagnetic conditions and 30 s during storm intervals, and the model outputs are recorded every 5 min.

Figure 3 shows the neutral mass density measurements during two separate CHAMP polar passes. Figure 3 (left column) shows mass density from the CHAMP accelerometers and FACs derived from the CHAMP magnetometer over the southern polar region between 13:41 and 13:56 UT, and Figure 3 (right column) corresponds to the satellite crossing over the northern polar region between 17:23 and 17:48 UT. According to Figure 2, there are two pulses of enhanced Joule heating and auroral precipitation centered around 12 UT and 17 UT, respectively. So the density anomalies were observed by CHAMP shortly after the high-latitude energy input peaks. The most distinct difference between these two CHAMP polar passes is that while the density anomaly over the southern polar cap around −80° MLAT was accompanied by intense FACs, the density anomaly over the Northern Hemisphere around 80° MLAT was absent of FACs. Thus, the northern polar cap density anomaly can be decoupled from FACs and local energy dissipation.

Figure 4 shows the TIEGCM outputs of neutral mass density and the height-integrated Joule heating prior to and during the CHAMP southern pass shown around 13:50 UT. The plotted neutral mass density corresponds to an altitude of 380 km, which is the average orbital altitude of CHAMP at that time. As shown in Figure 2, the hemispheric-integrated Joule heating starts to increase rapidly around 10:00 UT when IMF B_z turned southward. At 10:50 UT, increased Joule heating can be seen on the sunward side of the CHAMP trajectory. A modest density enhancement is also found equatorward of the main heating zone but no obvious density

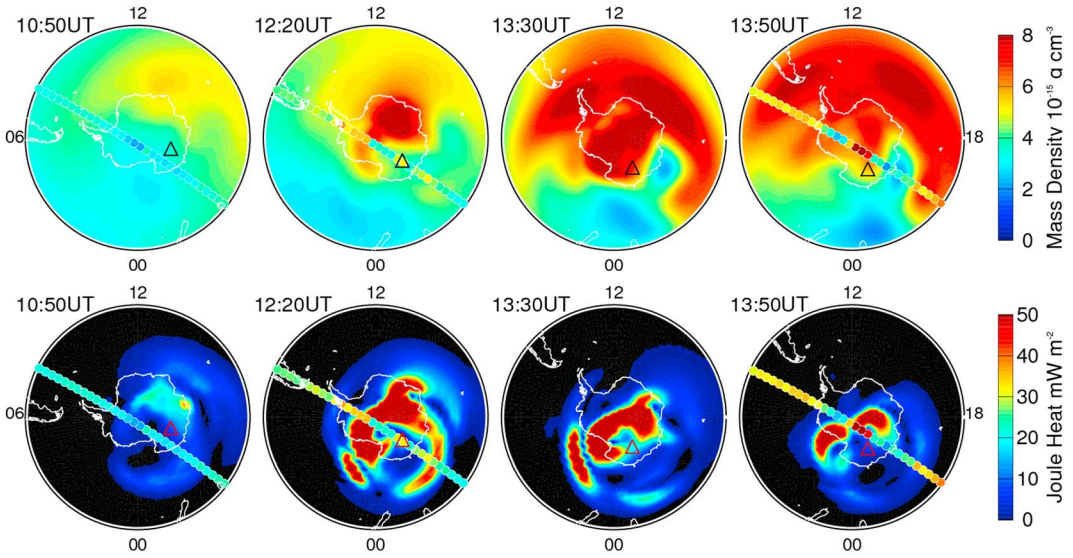

Figure 4. Maps of (top row) neutral mass density at 380 km and (bottom row) height-integrated Joule heating over the Southern Hemisphere. The small colored dots indicate the CHAMP trajectory, with the color of each dot corresponding to the mass density value measured by CHAMP using the color scale from Figure 4 (top row). The outer circle corresponds to 40°S, and the triangle in each map indicates the magnetic South Pole.

increase along the satellite track as indicated by the small colored dots. By 12:20 UT Joule heating has increased significantly around the auroral zone. Enhanced mass density is mostly located sunward of the CHAMP trajectory, and the satellite only encountered some modest increase associated with the tail of the tadpole shaped high mass density region over Antarctica. In addition to the region of increased mass density, a reduced mass density zone is formed at midlatitudes on the nightside. At 13:30 UT, about 20 min prior to the observed CHAMP polar cap density anomaly, a large density enhancement is present across the Antarctic continent above the region of strong Joule heating. But the density enhancement can also be clearly seen equatorward of Antarctica where there is no direct Joule heating dissipation. Again, two patches of reduced mass density are formed just off the Antarctic coast near dusk and on the nightside. Around 13:50 UT, CHAMP observed a large density anomaly near −80° MLAT. The simulation shows that the anomaly roughly coincides with a narrow band of intense Joule heating, which seems to have been significantly reduced over a time span of 20 min from 13:30 to 13:50 UT. The modeled density enhancement in central Antarctica is very similar to that in the CHAMP observations although the modeled value is somewhat smaller than the observed value. Farther equatorward of Antarctica, a modest density enhancement was observed by CHAMP. While the simulation depicts a similar midlatitude density enhancement, it overestimates the magnitude compared to observations. According to the simulation, the most intense density enhancement is located sunward of the CHAMP satellite track where Joule heating is largely absent.

Figure 5 shows the TIEGCM mass density and the height-integrated Joule heating maps before and during the CHAMP northern pass around 17:40 UT. At 11:40 UT, no significant density enhancement along the satellite track can be seen, neither by CHAMP nor in the simulation. Instead, a very modest density increase is located in the early afternoon sector above a region of increased Joule heating at that time. At 14:40 UT, weak and spotty Joule heating exists just sunward of the satellite track. The density enhancement can be found at midlatitudes in the prenoon sector, consistent with the CHAMP measurements. At 17:20 UT, more intense Joule heating appears near the dawnside auroral zone, yet enhanced density is mainly in the premidnight sector and at midlatitudes. Though enhanced density is also present on the dawnside, its main band resides equatorward of the heating zone. About 20 min later at 17:40 UT, it appears that the previous dawnside density enhancement has split into two patches: the portion poleward of the dawnside Joule heating zone has moved to near the north magnetic pole, whereas the equatorward density band has moved farther equatorward and also expanded in size. Over the same time period, the Joule heating pattern has changed very little,

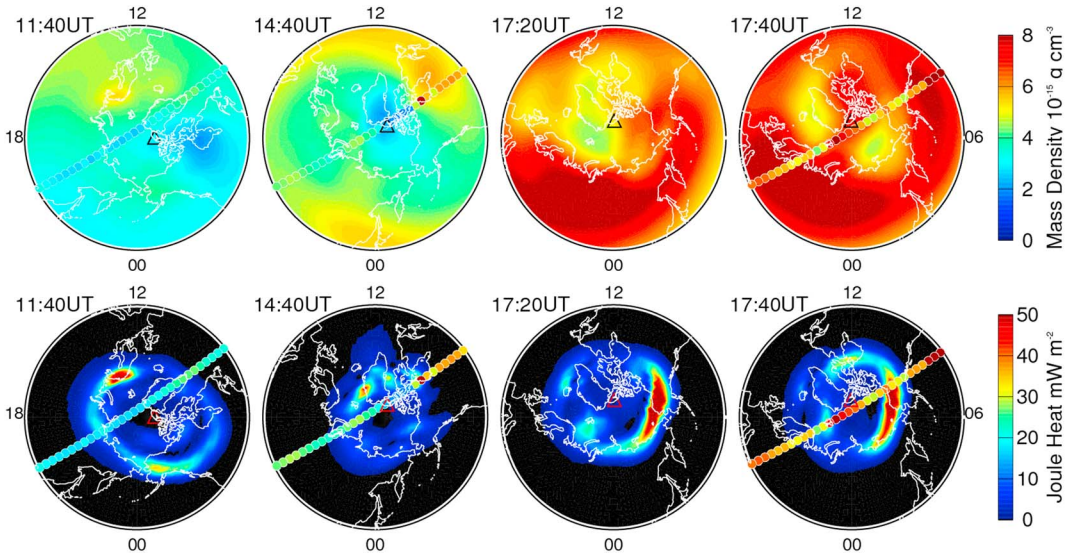

Figure 5. Similar to Figure 4 but for the Northern Hemisphere. The outer circle corresponds to 40°N, and the triangle indicates the magnetic North Pole.

and there is little energy dissipation over the polar cap where the density anomaly was observed by CHAMP. In addition to the polar cap, the simulation also exhibits density enhancements equatorward of the Joule heating zone, which is also consistent with the CHAMP observations but with overestimated values. Despite the complex and very dynamic redistribution of neutral mass density, our simulation seems to agree well with the CHAMP observations, at least qualitatively.

3. Discussion

It is apparent that the density variations have a complex relation to the Joule heating distribution. This occurs because dynamics rapidly redistributes the heat and changes the composition and temperature [e.g., *Rishbeth et al.*, 1987; *Lei et al.*, 2010]. In order to investigate some of the physical processes responsible for this complex relation, we show in Figure 6 the distributions of mass density (ρ), total number density (N), neutral temperature (T_N), and mean molecular mass ($\overline{m}$) at 380 km, along with the height-integrated Joule heating for the 1 h interval proceeding the CHAMP observed density anomaly in the Northern Hemisphere. For reference purpose, we also show the same quantities for the quiet time at 07:30 UT on 17 January. From a different perspective, latitude-height slices of Joule heating and of the change of mean molecular mass across the polar region in the dusk-dawn meridional plane are shown in Figures 7 and 8, along with winds and pressure-surface heights. In Figure 7 the colors indicate heating per unit mass, while the red contours in the lower thermosphere represent heating per unit volume. In Figure 8 the difference mean molecular mass shown by the colors is $\Delta\overline{m} = [\overline{m}(t,\theta,\varphi,z) - \overline{m}(t_0,z)]$, where $\overline{m}(t,\theta,\varphi,z)$ is the mean molecular mass at the given time t, latitude θ, longitude φ, and altitude z, and $\overline{m}(t_0,z)$ is the globally averaged mean molecular mass at the corresponding altitude z during the quiet time at 07:30 UT on 17 January. The colored dots, which are used to illustrate the displacement of individual air parcels, are discussed later. According to the perfect gas law, $P = NkT_N$, where P is the pressure, k is the Boltzmann constant, and N and T_N are anticorrelated with each other at a constant pressure level. However, at a fixed altitude as shown in Figure 6, the relationship between N and T_N becomes more complex due to three processes occurring that influence thermospheric variations.

First, heating increases the temperature and expands the atmosphere through barometric motion [i.e., *Rishbeth et al.*, 1969]. In this process, neutral mass density is positively correlated with temperature change at higher altitudes, though the detailed correlation may be modulated by variations of mean molecular mass [*Rishbeth and Müller-Wodarg*, 1999; *Lei et al.*, 2010].

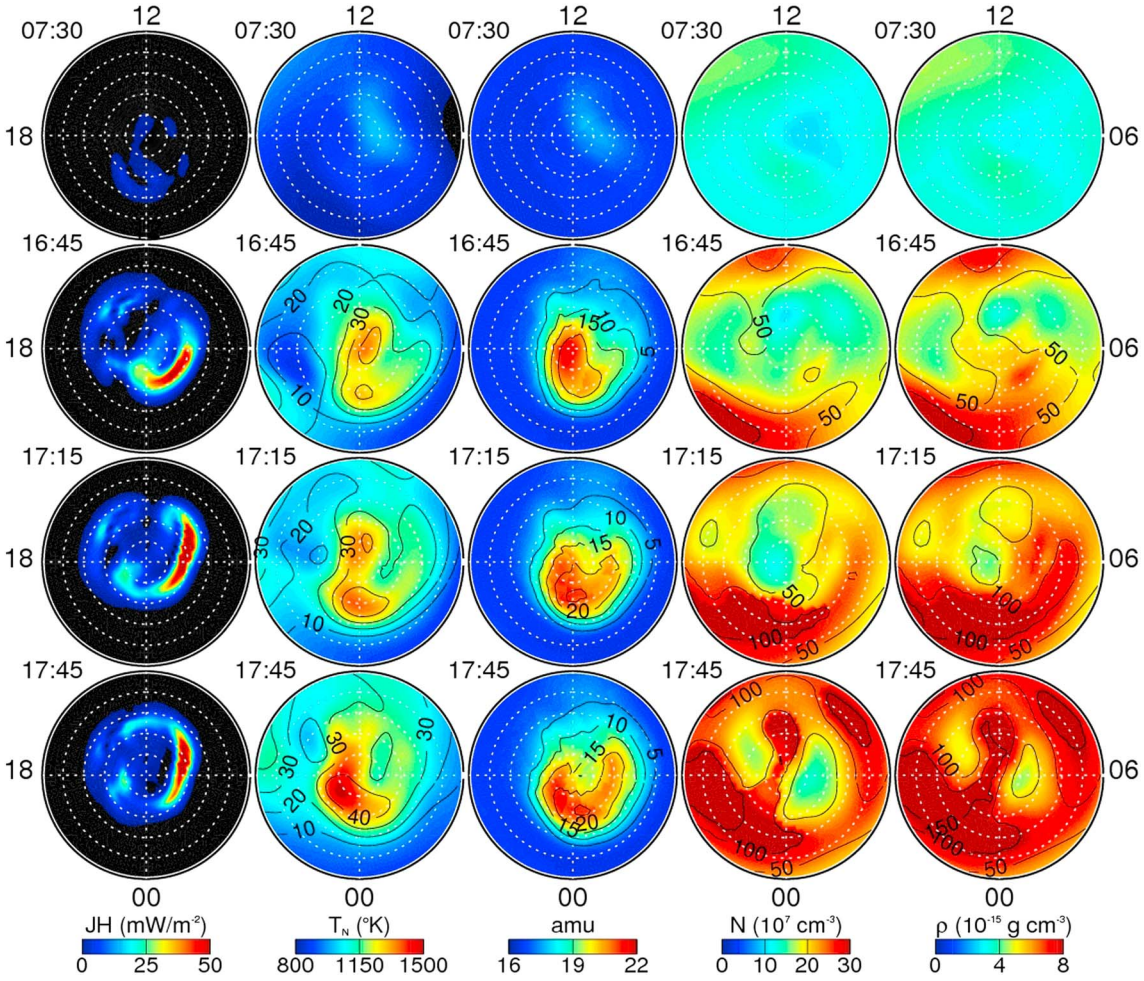

Figure 6. Maps of (first column) height-integrated Joule heating, (second column) neutral temperature, (third column) mean molecular mass in atomic mass units (1 amu = 1.66×10^{-27} kg), (fourth column) neutral number density, and (fifth column) neutral mass density. All maps are plotted at a fixed altitude of 380 km above 40°N. The contours represent the percent changes of neutral parameters with respect to their quiet time values shown in Figure 6 (top row).

Second, localized heating makes the air more buoyant so that it tends to rise and bring molecular-rich air to higher altitudes [*Fuller-Rowell et al.*, 1997]. Associated with this upwelling is horizontal outflow at higher altitudes and downflow at latitudes outside the heating region that act toward eliminating horizontal pressure gradients and maintaining horizontal uniformity of the density and the scale height, although horizontal gradients of pressure, density, and scale height are not totally eliminated. The temperature adjusts, partly through adiabatic changes associated with the vertical motions, so as to reduce horizontal variations of $T_N/\overline{m}$. Because $\overline{m}$ is horizontally nonuniform, T_N tends to be nonuniform owing to this circulation. *Lei et al.* [2010] showed how horizontal density variations at 400 km would be considerably greater if only the storm time temperature changes but not the composition changes (i.e., under the approximation of barometric motion) were taken into account in the hydrostatic relation. It is apparent in Figure 6 that both T_N and $\overline{m}$ are generally enhanced over the polar region by comparable amounts. The fact that the enhancements of T_N and $\overline{m}$ appear broadly over the polar region, whereas the height-integrated Joule heating is concentrated in the auroral region, may be due partly to horizontal spreading of the composition enhancements created by upwelling. But it is also due partly to the fact that it is primarily Joule heating at *F* region altitudes, and not total height-integrated Joule heating, that has the greatest impact on the temperature and composition at 380 km [e.g., *Deng et al.*, 2011; *Huang et al.*, 2012]. As shown in Figure 7, at 16:45 UT, intense heating (per unit mass) above 300 km near the North Pole is evident, even though most of the total Joule heat is deposited at *E* region heights at auroral latitudes between 70° and 75°N on the dawnside (right). The *F* region heating is only a minor (~10%) portion of the total Joule heating, and is comparable over the polar cap and

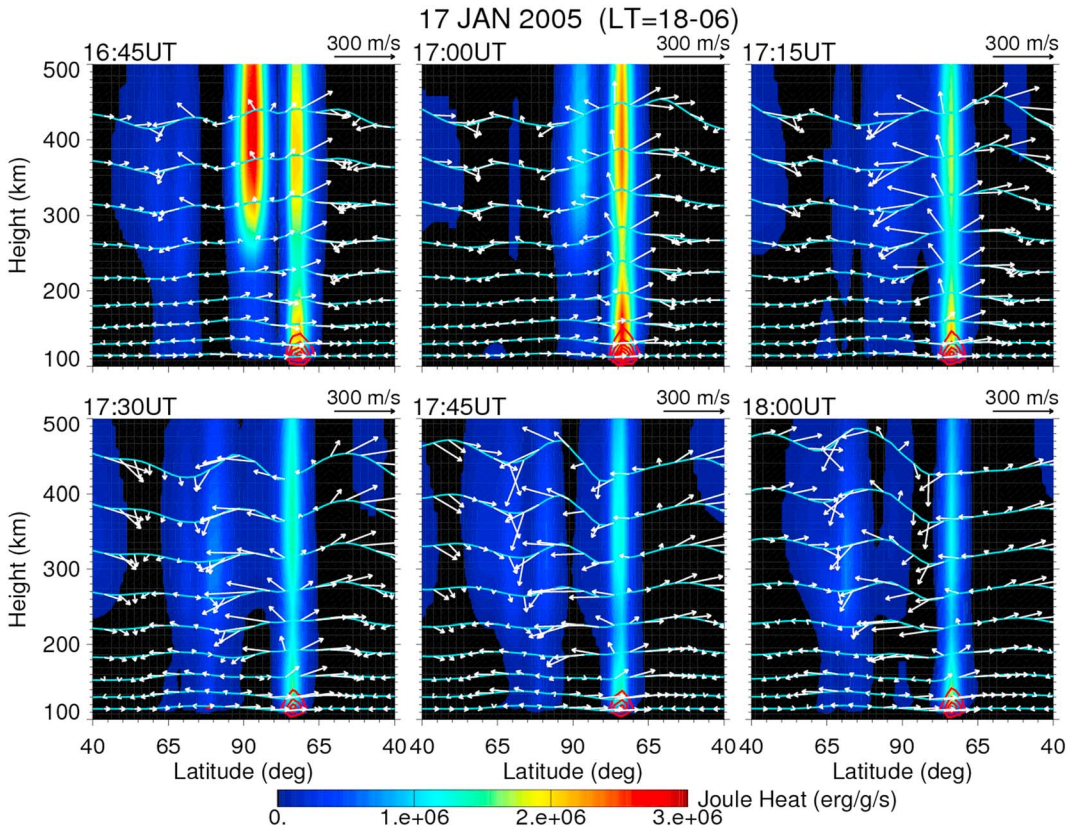

Figure 7. Vertical distributions of Joule heating along the dusk-dawn meridian at selected UT times, with the heating per unit mass represented by colors and the heating per unit volume plotted as contours. The cyan lines correspond to the heights of the pressure levels from −4 to 4, and the white arrows represent the meridional and vertical winds. Note that the plotted vertical winds are amplified by a factor of 5. Dawn is to the right and dusk to the left.

auroral zone, unlike the total Joule heating. The polar cap *F* region heating leading up to the time at 16:45 UT is responsible for the large increase of mean molecular mass in the polar cap, at this time seen in Figure 8.

The third main process affecting the high-altitude thermospheric variations is atmospheric gravity waves (AGWs) generated by the impulsive Joule heating. These AGWs are generated mainly in the lower thermosphere [*Richmond*, 1978] and propagate horizontally and vertically into the upper thermosphere as TADs, creating transient horizontal gradients. The associated vertical winds produce variations of T_N and $\overline{m}$ that are approximately out of phase, in contrast to the in-phase variations produced by the upwelling and downwelling induced by local Joule heating discussed above. The AGWs produce both augmentations and diminutions of density, so that an observed density peak represents not simply a density increase, but rather a local density increase that is flanked by density troughs. The AGWs and their effects are discussed in more detail later.

The variations seen in Figure 6 are a combination of these three processes. The storm time heating causes a general increase of T_N, N, and ρ. However, the increase in T_N is not uniform, nor does it maximize where the height-integrated Joule heating is located. Instead, T_N increases mainly over the central polar region where total Joule heating is relatively small, and only a modest T_N increase (about 200°K or 20% above the quiet time background) is found over the dawnside auroral zone where Joule heating is most intense. The mismatch between locations of high T_N and total height-integrated Joule heating peak is due to the disproportionate importance of *F* region Joule heating mentioned earlier, to adiabatic heating and cooling through vertical winds, to the presence of AGWs, to temporal lags between heating and thermospheric responses, and to spatial redistributions by horizontal winds. As explained by *Lei et al.* [2010], the density change at high altitude depends exponentially on the average change of scale height over the multiple scale heights existing between the main heating region and the high-altitude observing location, and this exponential effect dominates over local changes of T_N or $\overline{m}$. Since the scale height is proportional to $T_N/\overline{m}$, fractional changes of

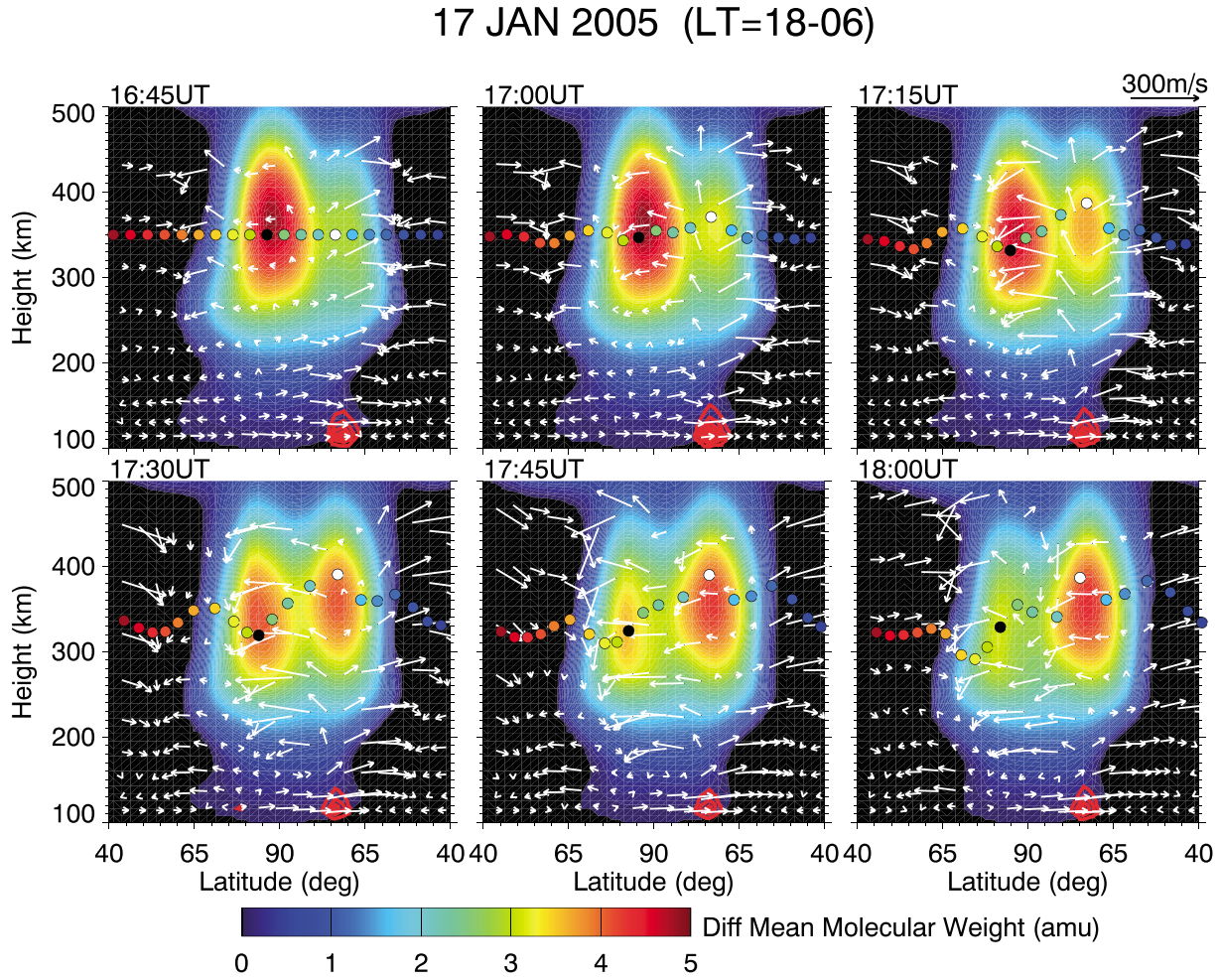

Figure 8. Vertical distributions of difference mean molecular mass along the dusk-dawn meridian at selected UT times. The red contours correspond to volumetric Joule heating intensity, and the white arrows represent the meridional and vertical winds. The colored dots are used to symbolize the individual air parcels, which are initially launched at 16:45 UT at a constant altitude of 350 km and evenly spaced in latitude.

either T_N or $\overline{m}$ below the observing height affect the density by comparable magnitudes, but in opposite directions. The fractional changes of T_N and $\overline{m}$ vary with height, but the values at 380 km indicated by the contours in Figure 6 can be considered representative of changes in the upper thermosphere. These contours show roughly comparable changes of T_N and $\overline{m}$, consistent with the tendency for vertical motions to reduce horizontal variations of the scale height, and thus of the ratio $T_N/\overline{m}$. However, the presence of gravity waves produces small-scale variations of $T_N/\overline{m}$. The patterns of N and ρ at 380 km are similar, albeit they differ by an amount proportional to $\overline{m}$. The largest increase in N is confined to the nightside, but there is also a gradual increase on the dawnside both poleward and equatorward of the main auroral zone where Joule heating intensifies. By 17:45 UT, N across the polar region has reached a magnitude more than 100% of its quiet time value. At the quiet time of 07:30 UT, the mean molecular mass is around 16 atomic mass units (amu) at 380 km, indicating that the neutral composition is dominated by atomic oxygen. During the active period from 16:45 to 17:45 UT, the mean molecular mass has increased above 20 amu as a result of upwelling of heavier, molecular-rich air from below. To further elucidate the dynamic response to high-latitude energy input, we also plot in Figures 7 and 8 the neutral winds (white arrows) and the heights (cyan contour lines) of pressure levels from −4 to 4. Note that since the vertical winds are generally much smaller than the meridional winds, we have amplified the wind vectors by a factor of 5 in the vertical direction in order to better depict the vertical wind variations. During the rapid increase of Joule heating that starts around 16:30 UT (see Figure 2) there is strong upper thermosphere heating in the polar cap at 16:45 UT as shown in Figure 7. At that time there is also intense Joule heating between 70° and 75° latitude in the dawnside (right) auroral

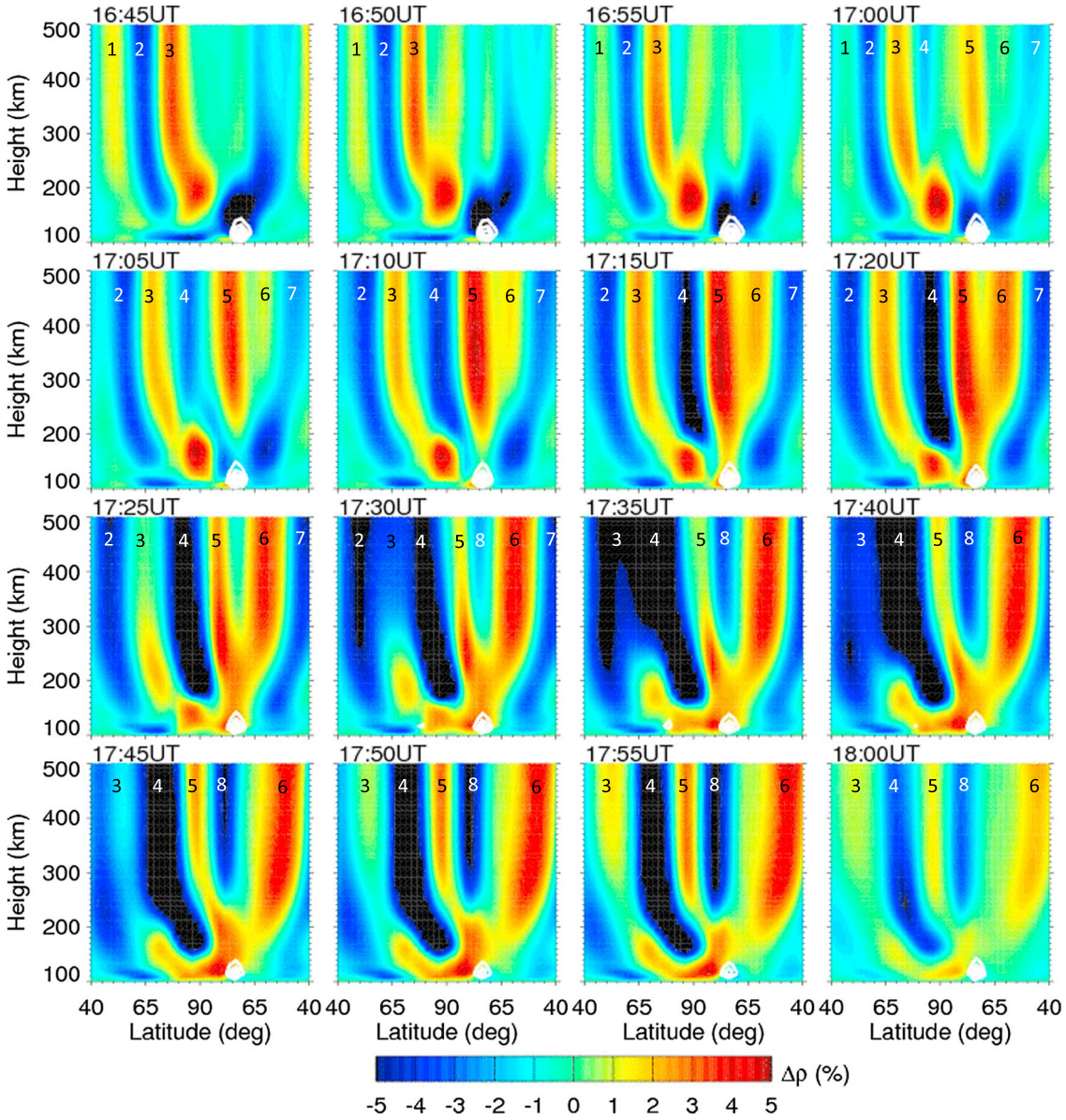

Figure 9. Vertical distributions of mass density variations (percent changes over a 10 min interval) along the dusk-dawn meridian. The Arabic numerals highlight the main phase fronts of AGWs.

zone. The volumetric heating indicated by the red contours is centered around 115 km in altitude where Pedersen conductivity peaks, while the heating per unit mass is also large in the upper thermosphere. Upward vertical winds start to develop in the upper thermosphere at this auroral location around 16:45 UT because of the heating. At 17:00 UT, the upward vertical winds in the auroral heating region further intensify. Temperature and composition changes below a given pressure level raise or lower the pressure level height to maintain hydrostatic equilibrium in the model. The variations of the pressure level height produce large latitudinal gradients, which in turn drive meridional winds. Between 17:00 and 17:30 UT the meridional winds above the heating region are divergent and couple with upward winds in a manner that preserves mass continuity. In fact, the upward winds at 17:00 UT and 17:15 UT produce adiabatic cooling that overcompensates the Joule heating, such that the upper level pressure surfaces subside. From 17:15 to 18:00 UT the contour lines of pressure level height above ~150 km become wavier, exhibiting a clear signature of propagating large-scale AGWs. The amplitude of the pressure level height fluctuations increases with altitude, which is another characteristic of AGWs that have been launched from lower altitudes and propagate upward [*Hines*, 1960].

In Figure 8 it is seen that the mean molecular mass gradually increases with time in regions of upward vertical winds and decreases in regions of downward winds. To highlight the transport effect by the winds, the colored dots symbolize the individual air parcels that are launched at 16:45 UT at a fixed altitude of 350 km and are initially evenly spaced in latitude. The air parcels are then transported by the meridional and vertical winds (the zonal wind effect is ignored). At 17:30 UT the black dot that is originally located near the primary maximum of the difference mean molecular mass has fallen to ~320 km, whereas the white dot near the secondary maximum of the difference mean molecular mass has risen to 390 km. By 18:00 UT the order of the original primary and secondary maxima of the difference mean molecular mass has reversed, and the latitudinal space between the colored dots becomes uneven due to the variations of the meridional winds experienced by the different air parcels. But the overall horizontal displacement is much smaller than the lateral motion of the mass density features over the polar region as illustrated in Figure 6, which travel at the AGW propagation speed. Thus, the formation of the polar cap density anomaly observed by CHAMP appears to be predominately a manifestation of the AGWs.

Further examination of AGWs is presented in Figure 9, which shows the dusk-dawn meridional distributions of the neutral mass density variations. The mass density variation is defined as $\Delta\rho(t,\theta,\varphi,z) = [\rho(t+\Delta t,\theta,\varphi,z) - \rho(t-\Delta t,\theta,\varphi,z)]/\overline{\rho}(t,z)$, where $\Delta t = 5$ min (e.g., the model output cadence) and $\overline{\rho}(t,z)$ is the globally averaged mass density at the given time t and height z. It should be noted that this quantity represents the normalized time rate of change (or "tendency") of mass density and is a mean to better capture the temporal variations associated with AGWs than the simple difference field with respect to the quiet time background (such as the contour plots shown in Figure 6). The white contours at the bottom of each panel correspond to the volumetric Joule heat distribution. The mass density tendencies form vertically tilted structures that are reminiscent of the phase fronts of AGWs generated by Joule heating [*Richmond*, 1978]. The main phase fronts are marked in Figure 9, and they apparently propagate away from the heating source both duskward/poleward and dawnward/equatorward in the form of TADs. Of particular interest to us are the positive density tendencies marked as 5 and 6, which first appear at 17:00 UT above the heating source on the dawnside. These two positive tendencies propagate laterally away from the heating region. By 17:45 UT, the duskward/poleward moving tendency 5 has just passed the north geographic pole, whereas the duskward/equatorward moving tendency 6 has reached 50° in latitude. A maximum density anomaly occurs when the tendency reverses from positive to negative. The positive density anomaly observed by CHAMP around 17:40 UT over the northern polar cap is associated with the positive tendency 5 during the preceding half hour and therefore is a result of a propagating TAD rather than generation by local Joule heating. Over the 1 h period from 17:00 to 18:00 UT, tendency 5 has moved about 20° in latitude from the dawnside at ~75°N to the duskside at ~85°N, corresponding to an average phase speed of ~650 m/s above 300 km where the AGW phase fronts become vertical. Our simulation has thus demonstrated the importance of nonlocal responses to energy inputs, in the form of TADs, for explaining the frequent lack of correspondence between the locations of energy inputs and density enhancements in the polar region. However, it is clear that TAD effects must be considered along with quasi-stationary dynamical effects associated with upwelling/outflow and barometric motion.

4. Conclusions

We carried out a quantitative assessment of high-latitude energy input and its partitioning in the polar cap during the 17 January 2005 geomagnetic storm based on various space- and ground-based observations with the aid of the AMIE data assimilation procedure. Among the main findings on magnetospheric energy input were as follows. 1. Consistent with studies of other storms, Joule heating is the dominant form of the high-latitude energy input compared to auroral precipitation. The ratio of the total hemisphere-integrated Joule heating versus the hemispheric-integrated auroral power is about 1.5 during quiet times and reaches a magnitude of as high as 9 during active times. 2. As defined by the CRB and FXB, the energy input over the polar cap only occasionally exceeds 50% of its hemispheric-integrated value. This occurs when the IMF is northward and the overall energy input is very low. 3. On average, the energy input over the polar cap accounts for 22–25% of the total hemispheric energy input. Therefore, we concluded that the polar cap is not the main location of magnetospheric energy input into the IT system. Had one used a simpler polar cap boundary as defined by the 78° MLAT circle, the energy input into the polar cap would be less than 10% of the total hemispheric energy input on average.It is worth noting that Finding (1) is not new; rather, it reaffirms the conclusion by several previous studies [e.g., *Akasofu*, 1981; *Ahn et al.*, 1983, 1989; *Knipp*

et al., 2004; *Lu et al*., 1996, 1998]. Findings (2) and (3) were based on a single event, and their generality has yet to be substantiated with more event studies under different solar wind and geomagnetic conditions.

To understand and elucidate the subsequent effects of high-latitude energy input on the thermosphere, particularly its relation with the observed polar cap density anomaly, we conducted a TIEGCM simulation to determine the underlying physical processes responsible for the formation of polar cap mass density anomalies as observed by the CHAMP satellite. Using time-varying, realistic specifications of plasma convection and auroral precipitation derived from AMIE, our model was able to reproduce the observed polar cap density anomaly, although quantitative model-data differences still exist. Further examination of simulation results revealed that three processes were mainly responsible for horizontal structuring of high-latitude temperature, composition, and density: (1) general temperature increase and atmospheric expansion (barometric motion) that led to high-altitude density increases, (2) upwelling induced by Joule heating that locally increased the mean molecular mass and led to coincident local temperature increases; and (3) large-scale AGWs were launched by the impulsive Joule heating energy input that propagated both poleward and equatorward and modulated thermospheric properties everywhere. The polar cap mass density anomalies observed by the CHAMP satellite during the storm were largely a result of large-scale atmospheric gravity waves. In general, depending on the location and time of the observation by a satellite with respect to the time history of energy input, density anomalies may or may not coincide with the heating source. Thus, caution must be taken when interpreting thermospheric dynamics based on localized observations.

Acknowledgments

We wish to acknowledge the International Real-time Magnetic Observatory Network for the INTERMAGNET magnetometer network, the Geophysical Institute of the University of Alaska for the Alaska magnetometer stations, the Solar-Terrestrial Environment Laboratory of the Nagoya University for the 210 magnetic meridian chain, the Finnish Meteorological Institute for the IMAGE chain, the Canadian Space Agency for CARISMA magnetometer network, the Space Plasma Environment and Radio Science (SPEARS) in the Department of Communication Systems at the Lancaster University for the SAMNET magnetometer chain, and the Danish Meterological Institute for the Greenland magnetometer stations. J. Posch at Augsburg College, A. Weather at Siena College, and O. Troshichev at the Arctic and Antarctic Research Institute in Russia provided additional ground magnetometer data used in the study. The SuperDARN radar data were provided by J.M. Ruohoniemi of the Virginia Tech SuperDARN group that is supported by the National Science Foundation (NSF). The DMSP particle data were prepared by Fred Rich at Air Force Research Laboratory, and the DMSP ion drift data were provided online by the University of Texas at Dallas at http://cindispace.utdallas.edu/DMSP/dmsp_data_at_utdallas.html. The POES data were processed and provided by Dave Evans at NOAA Space Weather Prediction Center. The ACE solar wind and IMF key parameters were obtained from the NASA CDAW website (http://cdaweb.gsfc.nasa.gov). This work was supported in part by the Heliophysics Guest Investigators program under NASA grant NNH09AK621, by the Geospace Research program under NASA grant NNX13AD64G, by the Living With a Star program under NASA grant NNX14AE08G, and by the U.S. Participating Investigator (USPI) Program under NASA grant NNX12AD26G. NCAR is sponsored by the NSF. The authors thank the International Space Science Institute in Bern, Switzerland, its staff and directors for supporting the ISSI Team "Field-Aligned Currents: Their Morphology, Evolution, Source Regions and Generators," from which this work was developed. We would like to acknowledge high performance computing support from Yellowstone (ark:/85065/d7wd3xhc) provided by NCAR's Computational and Information Systems Laboratory and sponsored by the NSF. The GUVI and SSUSI data used in this study are available online at http://guvi.jhuapl.edu/site/data/guvi-dataproducts.shtml and http://ssusi.

References

Ahn, B.-H., S.-I. Akasofu, and Y. Kamide (1983), The Joule heat production rate and the particle energy injection rate as a function of the geomagnetic indices *AE* and *AL*, *J. Geophys. Res.*, *88*, 6275–6287, doi:10.1029/JA088iA08p06275.

Ahn, B.-H., H. W. Kroehl, Y. Kamide, D. J. Gorney, S.-I. Akasofu, and J. R. Kan (1989), The auroral energy deposition over the polar ionosphere during substorms, *Planet. Space Sci.*, *37*, 239–252, doi:10.1016/0032-0633(89)90022-6.

Akasofu, S.-I. (1981), Energy coupling between the solar wind and the magnetosphere, *Space Sci. Rev.*, *28*, 121–193.

Akasofu, S.-I., and Y. Kamide (1976), Substorm energy, *Planet. Space Sci.*, *24*(3), 223–227, doi:10.1016/0032-0633(76)90019-2.

Baker, D. N., T. I. Pulkkinen, M. Hesse, and R. L. McPherron (1997), A quantitative assessment of energy storage and release in the Earth's magnetotail, *J. Geophys. Res.*, *102*, 7159–7168, doi:10.1029/96JA03961.

Baker, J. B., C. R. Clauer, A. J. Ridley, V. O. Papitashvili, M. J. Brittnacher, and P. T. Newell (2000), The nightside poleward boundary of the auroral oval as seen by DMSP and the Ultraviolet Imager, *J. Geophys. Res.*, *105*, 21,267–21,280, doi:10.1029/1999JA000363.

Brittnacher, M., M. Fillingim, G. Parks, G. Germany, and J. Spann (1999), Polar cap area and boundary motion during substorms, *J. Geophys. Res.*, *104*, 12,251–12,262, doi:10.1029/1998JA900097.

Bruinsma, S. L., and J. M. Forbes (2009), Properties of traveling atmospheric disturbances (TADs) inferred from CHAMP accelerometer observations, *Adv. Space Res.*, *23*, 369–376, doi:10.1016/j.asr.2008.10.031.

Bruinsma, S. L., and J. M. Forbes (2010), Large-scale traveling atmospheric disturbances (LSTADs) in the thermosphere inferred from CHAMP, GRACE, and SETA accelerometer data, *J. Atmos. Sol. Terr. Phys.*, *72*, 1057–1066.

Burns, A. G., T. L. Killeen, W. Deng, G. R. Carignan, and R. G. Roble (1995), Geomagnetic storm effects in the low- to middle-latitude upper thermosphere, *J. Geophys. Res.*, *100*, 14,673–14,691, doi:10.1029/94JA03232.

Chen, Y.-J., R. A. Heelis, and J. A. Cumnock (2015), Response of the ionospheric convection reversal boundary at high latitudes to changes in the interplanetary magnetic field, *J. Geophys. Res. Space Physics*, *120*, 5022–5034, doi:10.1002/2015JA021024.

Chisham, G., and M. P. Freeman (2004), An investigation of latitudinal transitions in the SuperDARN Doppler spectral width parameter at different magnetic local times, *Ann. Geophys.*, *22*, 1187–1202.

Chisham, G., M. P. Freeman, T. Sotirelis, R. A. Greenwald, M. Lester, and J.-P. Villain (2005), A statistical comparison of SuperDARN spectral width boundaries and DMSP particle precipitation boundaries in the morning sector ionosphere, *Ann. Geophys.*, *23*, 733–743, doi:10.5194/angeo-23-733-2005.

Chun, F. K., D. J. Knipp, M. G. McHarg, J. R. Lacey, G. Lu, and B. A. Emery (2002), Joule heating patterns as a function of polar cap index, *J. Geophys. Res.*, *107*(A7), 1119, doi:10.1029/2001JA000246.

Crowley, G., J. Schoendorf, R. G. Roble, and F. A. Marcos (1996), Cellular structures in the high-latitude thermosphere, *J. Geophys. Res.*, *101*, 211–223.

Crowley, G., T. J. Immel, C. L. Hackert, J. Craven, and R. G. Roble (2006), Effect of IMF B_Y on thermospheric composition at high and middle latitudes: 1. Numerical experiments, *J. Geophys. Res.*, *111*, A10311, doi:10.1029/2005JA011371.

Deng, Y., A. Maute, A. D. Richmond, and R. G. Roble (2009), Impact of electric field variability on Joule heating and thermospheric temperature and density, *Geophys. Res. Lett.*, *36*, L08105, doi:10.1029/2008GL036916.

Deng, Y., T. J. Fuller-Rowell, R. A. Akmaev, and A. J. Ridley (2011), Impact of the altitudinal Joule heating distribution on the thermosphere, *J. Geophys. Res.*, *116*, A05313, doi:10.1029/2010JA016019.

Emery, B. A., A. D. Richmond, H. W. Kroehl, C. D. Wells, and J. M. Ruohoniemi (1990), Electric potential patterns deduced for the SUNDIAL period of September 23–26, 1986, *Ann. Geophys.*, *8*, 339–408.

Forbes, J. M., G. Lu, S. Bruinsma, S. Nerem, and X. Zhang (2005), Thermosphere density variations due to the 15–24 April 2002 solar events from CHAMP/STAR accelerometer measurements, *J. Geophys. Res.*, *110*, A12S27, doi:10.1029/2004JA010856.

Foster, J. C., J.-P. St.-Maurice, and V. J. Abreu (1983), Joule heating at high latitudes, *J. Geophys. Res.*, *88*, 4885–4897, doi:10.1029/JA088iA06p04885.

Fuller-Rowell, T. J., and D. S. Evans (1987), Height-integrated Pedersen and Hall conductivity patterns inferred from the TIROS-NOAA satellite data, *J. Geophys. Res.*, *92*, 7606–7618, doi:10.1029/JA092iA07p07606.

jhuapl.edu/data_products. The CHAMP neutral mass density data were prepared by Eelco Doornbos at Delft University of Technology in Delft, the Netherlands, and can be obtained at http://thermosphere.tudelft.nl/accel-drag/index.php. The TIEGCM and AMIE results in this study are archived on NCAR's High Performance Storage System and are available on request to Gang Lu (ganglu@ucar.edu).

Fuller-Rowell, T. J., M. V. Codrescu, R. G. Roble, and A. D. Richmond (1997), How does the thermosphere and ionosphere react to a geomagnetic storm?, in *Magnetic Storm*, *Geophys. Monogr. Ser.*, vol. 98, pp. 203–205, AGU, Washington, D. C.

Fuller-Rowell, T. J., T. Matsuo, V. M. Codrescu, and F. A. Marcos (1999), Modeling thermospheric neutral density waves and holes in response to high latitude forcing, *Adv. Space Res.*, *24*, 1447–1458.

Hagan, M. E., and J. M. Forbes (2002), Migrating and nonmigrating diurnal tides in the middle and upper atmosphere excited by tropospheric latent heat release, *J. Geophys. Res.*, *107*(D24), 4754, doi:10.1029/2001JD001236.

Hagan, M. E., and J. M. Forbes (2003), Migrating and nonmigrating semidiurnal tides in the upper atmosphere excited by tropospheric latent heat release, *J. Geophys. Res.*, *108*(A2), 1062, doi:10.1029/2002JA009466.

Hardy, D. A., M. S. Gussenhoven, and E. Holeman (1985), A statistical model of auroral electron precipitation, *J. Geophys. Res.*, *90*, 4229–4248, doi:10.1029/JA090iA05p04229.

Hardy, D. A., W. McNeil, M. S. Gussenhoven, and D. Brautigam (1991), A statistical model of auroral ion precipitation: 2. Functional representation of the average patterns, *J. Geophys. Res.*, *96*, 5539–5547, doi:10.1029/90JA02451.

Hines, C. O. (1960), Internal atmospheric gravity waves at ionospheric heights, *Can. J. Phys.*, *38*(11), 1441–1481, doi:10.1139/p60-150.

Huang, C. Y., Y.-J. Su, E. K. Sutton, D. R. Weimer, and R. L. Davidson (2014), Energy coupling during the August 2011 magnetic storm, *J. Geophys. Res. Space Physics*, *119*, 1219–1232, doi:10.1002/2013JA019297.

Huang, Y., A. D. Richmond, Y. Deng, and R. Roble (2012), Height distribution of Joule heating and its influence on the thermosphere, *J. Geophys. Res.*, *117*, A08334, doi:10.1029/2012JA017885.

Hubert, B., A. T. Aikio, O. Amm, T. Pitkänen, K. Kauristie, S. E. Milan, S. W. H. Cowley, and J.-C. Gérard (2010), Comparison of the open-closed field line boundary location inferred using IMAGE-FUV SI12 images and EISCAT radar observations, *Ann. Geophys.*, *28*, 883–892, doi:10.5194/angeo-28-883-2010.

Kamide, Y., S. Kokubun, L. F. Bargatze, and L. A. Frank (1999), The size of the polar cap as an indicator of substorm energy, *Phys. Chem. Earth, Part C, Sol.-Terr. Planet. Sci.*, *24*(1-3), 119–127.

Kauristie, K., J. Weygand, T. I. Pulkkinen, J. S. Murphree, and P. T. Newell (1999), Size of the auroral oval: UV ovals and precipitation boundaries compared, *J. Geophys. Res.*, *104*, 2321–2331, doi:10.1029/1998JA900046.

Knipp, D., S. Eriksson, L. Kilcommons, G. Crowley, J. Lei, M. Hairston, and K. Drake (2011), Extreme Poynting flux in the dayside thermosphere: Examples and statistics, *Geophys. Res. Lett.*, *38*, L16102, doi:10.1029/2011GL048302.

Knipp, D. J., W. K. Tobiska, and B. A. Emery (2004), Direct and indirect thermospheric heating sources for sola cycle 21–23, *Sol. Phys.*, *224*, 495–505, doi:10.1007/s11207-005-6393-4.

Lei, J., J. P. Thayer, A. G. Burns, G. Lu, and Y. Deng (2010), Wind and temperature effects on thermosphere mass density response to the November 2004 geomagnetic storm, *J. Geophys. Res.*, *115*, A05303, doi:10.1029/2009JA014754.

Liu, R., H. Lühr, and S.-Y. Ma (2010), Storm-time related mass density anomalies in the polar cap as observed by CHAMP, *Ann. Geophys.*, *28*(1), 165–180.

Liu, X., J. P. Thayer, A. Burns, W. Wang, and E. Sutton (2014), Altitude variations in the thermosphere mass density response to geomagnetic activity during the recent solar minimum, *J. Geophys. Res. Space Physics*, *119*, 2160–2177, doi:10.1002/2013JA019453.

Liuzzo, L. R., A. J. Ridley, N. J. Perlongo, E. J. Mitchell, M. Conde, D. L. Hampton, W. A. Bristow, and M. J. Nicolls (2015), High-latitude ionospheric drivers and their effects on wind patterns in the thermosphere, *J. Geophys. Res. Space Physics*, *120*, 715–735, doi:10.1002/2014JA020553.

Longden, N., G. Chisham, M. P. Freeman, G. A. Abel, and T. Sotirelis (2010), Estimating the location of the open-closed magnetic field line boundary from auroral images, *Ann. Geophys.*, *28*, 1659–1678.

Lu, G., et al. (1996), High-latitude ionospheric electrodynamics as determined by the assimilative mapping of ionospheric electrodynamics procedure for the conjunctive SUNDIAL/ATLAS 1/GEM period of March 28–29, 1992, *J. Geophys. Res.*, *101*, 26,697–26,718, doi:10.1029/96JA00513.

Lu, G., et al. (1998), Global energy deposition during the January 1997 magnetic cloud event, *J. Geophys. Res.*, *103*, 11,685–11,694, doi:10.1029/98JA00897.

Lu, G., A. D. Richmond, J. M. Ruohoniemi, R. A. Greenwald, M. Hairston, F. J. Rich, and D. S. Evans (2001), An investigation of the influence of data and model inputs on assimilative mapping of ionospheric electrodynamics, *J. Geophys. Res.*, *106*, 417–433, doi:10.1029/2000JA000606.

Lühr, H., M. Rother, W. Kohler, P. Ritter, and L. Grunwaldt (2004), Thermospheric up-welling in the cusp region: Evidence from CHAMP observations, *Geophys. Res. Lett.*, *31*, L06805, doi:10.1029/2003GL019314.

Mayr, H. G., I. Harris, F. A. Herrero, N. W. Spencer, F. Varosi, and W. D. Pesnell (1990), Thermospheric gravity waves: Observations and interpretation using the transfer function model (TFM), *Space Sci. Rev.*, *54*, 297–375.

Milan, S. E., M. Lester, S. W. H. Cowley, J. Moen, P. E. Sandholt, and C. J. Owen (1999), Meridian-scanning photometer, coherent HF radar, and magnetometer observations of the cusp: A case study, *Ann. Geophys.*, *17*, 159–172, doi:10.1007/s00585-999-0159-5.

Milan, S. E., M. Lester, S. W. H. Cowley, K. Oksavik, M. Brittnacher, R. A. Greenwald, G. Sofko, and J.-P. Villain (2003), Variations in the polar cap area during two substorm cycles, *Ann. Geophys.*, *21*, 1121–1140.

Millward, G. H., R. J. Moffett, S. Quegan, and T. J. Fuller-Rowell (1993), Effects of an atmospheric gravity wave on the midlatitude ionospheric *F* layer, *J. Geophys. Res.*, *98*, 19,173–19,179, doi:10.1029/93JA02093.

Mishin, V. M. (1990), The magnetogram inversion technique and some applications, *Space Sci. Rev.*, *57*, 83–163, doi:10.1007/BF00217429.

Mitchell, E. J., P. T. Newell, J. W. Gjerloev, and K. Liou (2013), OVATION-SM: A model of auroral precipitation based on SuperMAG generalized auroral electrojet and substorm onset times, *J. Geophys. Res. Space Physics*, *118*, 3747–3759, doi:10.1002/jgra.50343.

Newell, P. T., and C.-I. Meng (1988), The cusp and the cleft/boundary layer: Low-altitude identification and statistical local time variation, *J. Geophys. Res.*, *93*(A12), 14,549–14,556, doi:10.1029/JA093iA12p14549.

Newell, P. T., Y. I. Feldstein, Y. I. Galperin, and C.-I. Meng (1996), The morphology of nightside precipitation, *J. Geophys. Res.*, *101*, 10,737–10,748, doi:10.1029/95JA03516.

Newell, P. T., T. Sotirelis, and S. Wing (2009), Diffuse, monoenergetic, and broadband aurora: The global precipitation budget, *J. Geophys. Res.*, *114*, A09207, doi:10.1029/2009JA014326.

Newell, P. T., T. Sotirelis, K. Liou, A. R. Lee, S. Wing, J. Green, and R. Redmon (2010), Predictive ability of four auroral precipitation models as evaluated using Polar UVI global images, *Space Weather*, *8*, S12004, doi:10.1029/2010SW000604.

Prölss, G. W. (1995), Ionospheric *F*-region storms, in *Handbook of Atmospheric Electrodynamics*, edited by H. Volland, pp. 195–248, CRC Press, Boca Raton, Fla.

Prölss, G. W. (1997), Magnetic storm associated perturbations of the upper atmosphere, in *Magnetic Storms*, *Geophys. Monogr. Ser.*, vol. 98, pp. 227–241, AGU, Washington, D. C.

Qian, L., S. C. Solomon, and M. G. Mlynczak (2010), Model simulation of thermospheric response to recurrent geomagnetic forcing, *J. Geophys. Res.*, *115*, A10301, doi:10.1029/2010JA015309.

Qian, L., A. G. Burns, B. A. Emery, B. Foster, G. Lu, A. Maute, A. D. Richmond, R. G. Roble, S. C. Solomon, and W. Wang (2013), The NCAR TIE-GCM: A community model of the coupled thermosphere/ionosphere system, in *Modeling the Ionosphere-Thermosphere System*, *Geophys. Monogr. Ser.*, vol. 201, edited by J. Huba, R. Schunk, and G. Khazanov, pp. 73–83, AGU, Washington, D. C., doi:10.1029/2012GM001297 (also published online in 2014 by John Wiley, Chichester, U. K., doi:10.1002/9781118704417.ch7).

Richmond, A. D. (1978), Gravity wave generation, propagation, and dissipation in the thermosphere, *J. Geophys. Res.*, *83*, 4131–4145, doi:10.1029/JA083iA09p04131.

Richmond, A. D., and Y. Kamide (1988), Mapping electrodynamic features of the high-latitude ionosphere from localized observations: Technique, *J. Geophys. Res.*, *93*, 5741–5759.

Richmond, A. D., and G. Lu (2000), Upper-atmospheric effects of magnetic storms: A brief tutorial, *J. Atmos. Sol. Terr. Phys.*, *62*, 1115–1127.

Richmond, A. D., and S. Matsushita (1975), Thermospheric response to a magnetic substorm, *J. Geophys. Res.*, *80*, 2839–2850, doi:10.1029/JA080i019p02839.

Richmond, A. D., et al. (1988), Mapping electrodynamic features of the high-latitude ionosphere from localized observations: Combined incoherent-scatter radar and magnetometer measurements for January 18–19, 1984, *J. Geophys. Res.*, *93*, 5760–5776, doi:10.1029/JA093iA06p05760.

Richmond, A. D., E. C. Ridley, and R. G. Roble (1992), A thermosphere/ionosphere general circulation model with coupled electrodynamics, *Geophys. Res. Lett.*, *19*, 601–604, doi:10.1029/92GL00401.

Rishbeth, H. (1991), *F*-region storms and thermospheric dynamics, *J. Geomagn. Geoelectr.*, *43*, 513–524.

Rishbeth, H., and I. C. F. Müller-Wodarg (1999), Vertical circulation and thermospheric composition: A modeling study, *Ann. Geophys.*, *17*, 794–805, doi:10.1007/s00585-999-0794-x.

Rishbeth, H., R. J. Moffett, and G. J. Bailey (1969), Continuity of air motion in the mid-latitude thermosphere, *J. Atmos. Terr. Phys.*, *31*, 1035–1047.

Rishbeth, H., T. J. Fuller-Rowell, and A. S. Roger (1987), *F*-layer storms and thermospheric composition, *Phys. Scr.*, *36*(2), 327–336.

Schunk, R. W., and J. J. Sojka (1996), Ionosphere-thermosphere space weather issues, *J. Atmos. Sol. Terr. Phys.*, *58*, 1527–1574, doi:10.1016/0021-9169(96)00029-3.

Sotirelis, T., J. M. Ruohoniemi, R. J. Barnes, P. T. Newell, R. A. Greenwald, J. P. Skura, and C.-I. Meng (2005), Comparison of SuperDARN radar boundaries with DMSP particle precipitation boundaries, *J. Geophys. Res.*, *110*, A06302, doi:10.1029/2004JA010732.

Thayer, J. P., X. Liu, J. Lei, M. Pilinski, and A. G. Burns (2012), The impact of helium on thermosphere mass density response to geomagnetic activity during the recent solar minimum, *J. Geophys. Res.*, *117*, A07315, doi:10.1029/2012JA017832.

Waters, C., B. Anderson, R. Greenwald, R. Barnes, and J. Ruohoniemi (2004), High-latitude Poynting flux from combined Iridium and SuperDARN data, *Ann. Geophys.*, *22*, 2861–2875, doi:10.5194/angeo-22-2861-2004.

Weimer, D. R. (2005), Improved ionospheric electrodynamic models and application to calculating Joule heating rates, *J. Geophys. Res.*, *110*, A05306, doi:10.1029/2004JA010884.

Xiong, C., and H. Lühr (2014), An empirical model of the auroral oval derived from CHAMP field-aligned current signatures—Part 2, *Ann. Geophys.*, *32*, 623–631, doi:10.5194/angeo-32-623-2014.

Zhang, Y., and L. J. Paxton (2008), An empirical *Kp*-dependent global auroral model based on TIMED/GUVI FUV data, *J. Atmos. Sol. Terr. Phys.*, *70*, 1231–1242.